Analysis of electrostatic stability and ordering in quaternary perovskite solid solutions

Clovis Caetano,[1,2,*] Keith T. Butler,[2] and Aron Walsh[2,3]

[1]*Universidade Federal da Fronteira Sul, Realeza, PR 85770-000, Brazil*

[2]*Centre for Sustainable Chemical Technologies and Department of Chemistry, University of Bath,
Claverton Down, Bath BA2 7AY, United Kingdom*

[3]*Global E³ Institute and Department of Materials Science and Engineering, Yonsei University, Seoul 120-749, Korea*

There are three distinct classes of perovskite structured metal oxides, defined by the charge states of the cations: $A^I B^V O_3$, $A^{II} B^{IV} O_3$, and $A^{III} B^{III} O_3$. We investigated the stability of cubic quaternary solid solutions ABO_3-$A'B'O_3$ using a model of point-charge lattices. The mixing enthalpies were calculated and compared for the three possible types of combinations of the compounds, both for the random alloys and the ground-state-ordered configurations. The mixing enthalpy of the $(I,V)O_3$-$(III,III)O_3$ alloy is always larger than the other alloys. We found that, different from homovalent alloys, for these heterovalent alloys a lattice constant mismatch between the constituent compounds could contribute to stabilize the alloy. At low temperatures, the alloys present a tendency to spontaneous ordering, forming superlattices consisting of alternated layers of ABO_3 and $A'B'O_3$ along the [110] direction.

I. INTRODUCTION

Compounds which crystallize in the perovskite structure, i.e., the structure related to the mineral $CaTiO_3$, can present many important physical properties, such as giant magnetoresistance [1], ferroelectricity [2], superconductivity [3], proton conductivity [4], and catalytic activity [5]. Such properties make the perovskites one of the most studied families of chemical compounds, both from a theoretical point of view and for applications [6]. In its ideal structure, a perovskite oxide ABO_3 presents a cubic phase formed by two interpenetrating sublattices, with the oxygen anions forming octahedral bonds with the smaller cations B, while the larger cations A are 12-fold coordinated. In general, the cubic structure is slightly distorted, and this deviation depends on the Goldschmidt tolerance factor $t = (r_A + r_O)/\sqrt{2}(r_B + r_O)$, where r_A, r_B, and r_O are the ionic radii. The cubic phase is formed when t is in the range between 0.9 and 1 [7]. Aside from cubic, perovskite compounds can also be found in other phases. As an example, the compound $NaNbO_3$, a high-efficiency photocatalyst for H_2 generation, is cubic at high temperatures, but at low temperatures presents several structural transitions to tetragonal, orthorhombic, and rhombohedral phases, which can be associated with ferroelectric and antiferroelectric instabilities [8].

Although the simple perovskite oxides ABO_3 have important practical interest, most of the perovskite compounds that have received more attention for technological applications are their solid solutions. Given the diversity of the properties of the perovskites, alloying two different compounds could produce materials with new and useful properties. Pseudobinary perovskite alloys $(AA')BO_3$ and $A(BB')O_3$, in which the mixture of cations takes place in only one sublattice, have been extensively studied, both experimental and theoretically. Bellaiche *et al.*, e.g., studied the energetic, structural, and dielectric properties of different perovskite

alloys [9]. In a more recent work, Armiento *et al.* investigated the piezoelectric performance and thermodynamic stability of a large chemical space of perovskite alloys [10]. Although less studied, quaternary perovskite alloys such as $(AA')(BB')O_3$, in which the cations in both sublattices can be mixed, have attracted some attention in the past decade. Xu *et al.*, e.g., analyzed the crystal structure and stability of $NaNbO_3$-$SrTiO_3$ alloy [11]. It is also possible to produce perovskite anion alloys, with oxynitrides the most studied member of this class [12]. One interesting aspect of complex perovskite compounds is the possibility of ordering of the cations within the sublattices. It is important because the physical properties of ordered compounds could be different of those of the random alloys. Chen *et al.*, e.g., showed that the electronic structure of $(SrTiO_3)_{1-x}(LaCrO_3)_x$ alloy can be tuned by controlling the cation arrangement [13]. It is not simple to predict if an alloy would present ordered phases and, if so, which kind of order, since it depends, among other things, on the cationic sizes and charge differences, bond valence, and tolerance factor [14–20].

In this paper, we study the stability of quaternary perovskite alloys ABO_3-$A'B'O_3$, where A and A' as well as B and B' are cations with different formal charges. The diagram in Fig. 1 shows the three possible solid solutions that result of mixing the pure perovskite compounds. Note that, since the alloys are heterovalent, in order to maintain a neutrally charged system, the compositions in the two sublattices must be the same. A solid solution with composition x could be represented by the expressions $A_{1-x}A'_x B_{1-x}B'_x O_3$ or $(1 - x)ABO_3$-$xA'B'O_3$. Through this text we will consider that the composition terms are implicit, so the last expression will be written simply ABO_3-$A'B'O_3$ or, more often, in terms of the cation valences, like in Fig. 1. In Table I, we give some examples of the three types of quaternary alloys. We consider in this work only electrostatic interactions among the ions, that is, point-charge alloys. This approach has already been efficiently used to study perovskite oxides [21–23] as well as spinel oxides [24,25]. Belaiche *et al.* showed that the electrostatic interactions among cations are more important than relaxation in the stability of heterovalent perovskite alloys
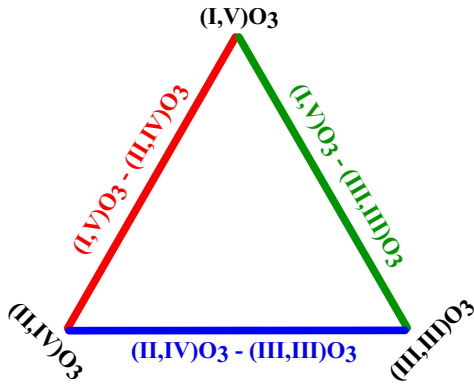
*ccaetano@uffs.edu.br

FIG. 1. Diagram representing the three types of quaternary perovskite alloys. The vertexes of the triangle are the pure perovskite compounds and the color lines represent the joint alloys.

[9]. Besides, electrostatic energy calculations have been often used to determine qualitative trends of structural preference in ordered alloys [26]. As it was pointed out above, perovskite alloys can be stable in different phases, depending on the end pure compounds, temperature, pressure, composition, etc., since this kind of study can be very complex. However, for the sake of simplicity, in this work we only consider the ideal cubic structure, which should be a good starting point for the understanding of the stability of the alloys.

II. COMPUTATIONAL DETAILS

The internal energy of an ionic crystal can be divided in two contributions [34]:

$$U = U^{\text{Coulomb}} + U', \tag{1}$$

where U^{Coulomb} is the electrostatic energy, also called Madelung energy and U' represents all the other contributions (repulsive interaction, van der Waals energy, vibrational energy, etc). In this work, we consider only the first term in internal energy, i.e., we represent the system as a lattice of point charges with electrostatic interactions between ions given by [35,36]

$$U_{ij}^{\text{Coulomb}} = k\frac{q_i q_j}{r_{ij}}, \tag{2}$$

where q_i and q_j are the formal charges of the ions, r_{ij} is the distance between them, and k is a dimensional constant. The formal charges of the ions can assume the following values, in atomic units: $q_A = +1, +2,$ or $+3$, $q_B = +5, +4,$ or $+3$

TABLE I. Examples of quaternary perovskite alloys synthesized experimentally.

Type	Examples
(I,V)O$_3$-(II,IV)O$_3$	NaNbO$_3$-SrTiO$_3$ [11,27,28]
	KNbO$_3$-SrTiO$_3$ [29]
	NaNbO$_3$-BaTiO$_3$ [30]
(I,V)O$_3$-(III,III)O$_3$	KNbO$_3$-LaFeO$_3$ [31]
(II,IV)O$_3$-(III,III)O$_3$	SrTiO$_3$-LaAlO$_3$ [32]
	SrTiO$_3$-LaCrO$_3$ [33]

and $q_O = -2$. The total electrostatic energy of the system is evaluated by summing the interactions (2) over all pairs, considering the periodicity of the system, what is done using the method of Ewald [37]. All the energy calculations were performed using GULP code [38]. As only electrostatic interactions were considered, no ion relaxation was permitted, that is, the ions were kept fixed.

In order to simulate the quaternary solid solution $(1 - x)ABO_3$ - $xA'B'O_3$, we calculated the energies of different configurations of the alloy in the entire range of composition, as will be explained in the following. The lattice constant of a cubic alloy depends on its composition and was determined by using the Vegard's law [39]

$$a = (1 - x)a_1 + xa_2, \tag{3}$$

where a_1 and a_2 are the lattice parameters of the pure compounds ABO_3 and $A'B'O_3$, respectively. For each alloy configuration k with total energy U_k, the respective enthalpy of mixing was calculated using the relation

$$\Delta H_k = U_k - (1 - x)U_{ABO_3} - xU_{A'B'O_3}, \tag{4}$$

where U_{ABO_3} and $U_{A'B'O_3}$ are the energies of the end pure compounds.

We consider in this work two approaches for the analysis of the system:

(1) *Random alloy*. Considering only the configurations k with a specific composition, the enthalpy of mixing of the alloy at the same composition can be determined by the expression [40]

$$\Delta H = \frac{\sum_k \Delta H_k g_k e^{-U_k/k_B T}}{\sum_{k'} g_{k'} e^{-U_{k'}/k_B T}}, \tag{5}$$

where the degeneracy g_k represents the number of configurations with the same energy U_k, and k_B is the Boltzmann constant. At high temperatures, Eq. (5) is reduced to the average of the enthalpies of mixing, weighted by the degeneracies. We used a $2 \times 2 \times 2$ supercell, which corresponds to 8 cations in each sublattice and a total of 40 atoms. The SOD code was employed to determine the nonequivalent configurations and their respective degeneracies [40]. For the supercell used, 76 nonequivalent configurations were found for the entire range of composition, although some of these configurations could have very close energies since only electrostatic interactions were taken into account. In order to make the model more realistic at finite temperatures, instead of using the formal charges q_i in Eq. (2), we considered effective charges $\tilde{q}_i$ with a 30% deviation from the nominal charges, i.e., $\tilde{q}_i = 0.7q_i$. This is equivalent to rescaling Eq. (2) with a dielectric constant ϵ that provides a screening effect on the Coulomb interaction. The enthalpy of mixing for the discrete compositions was calculated by the average (5), and the results were then fitted using the subregular solution expression

$$\Delta H(x) = \Omega x(1 - x), \tag{6}$$

where $\Omega = \alpha + \beta x$, α and β being fitting parameters. Although we considered only electrostatic interactions, the application of a composition-dependent parameter Ω allowed us to go beyond regular solution theory and consider possible asymmetries in the enthalpy of mixing [41]. The effect of
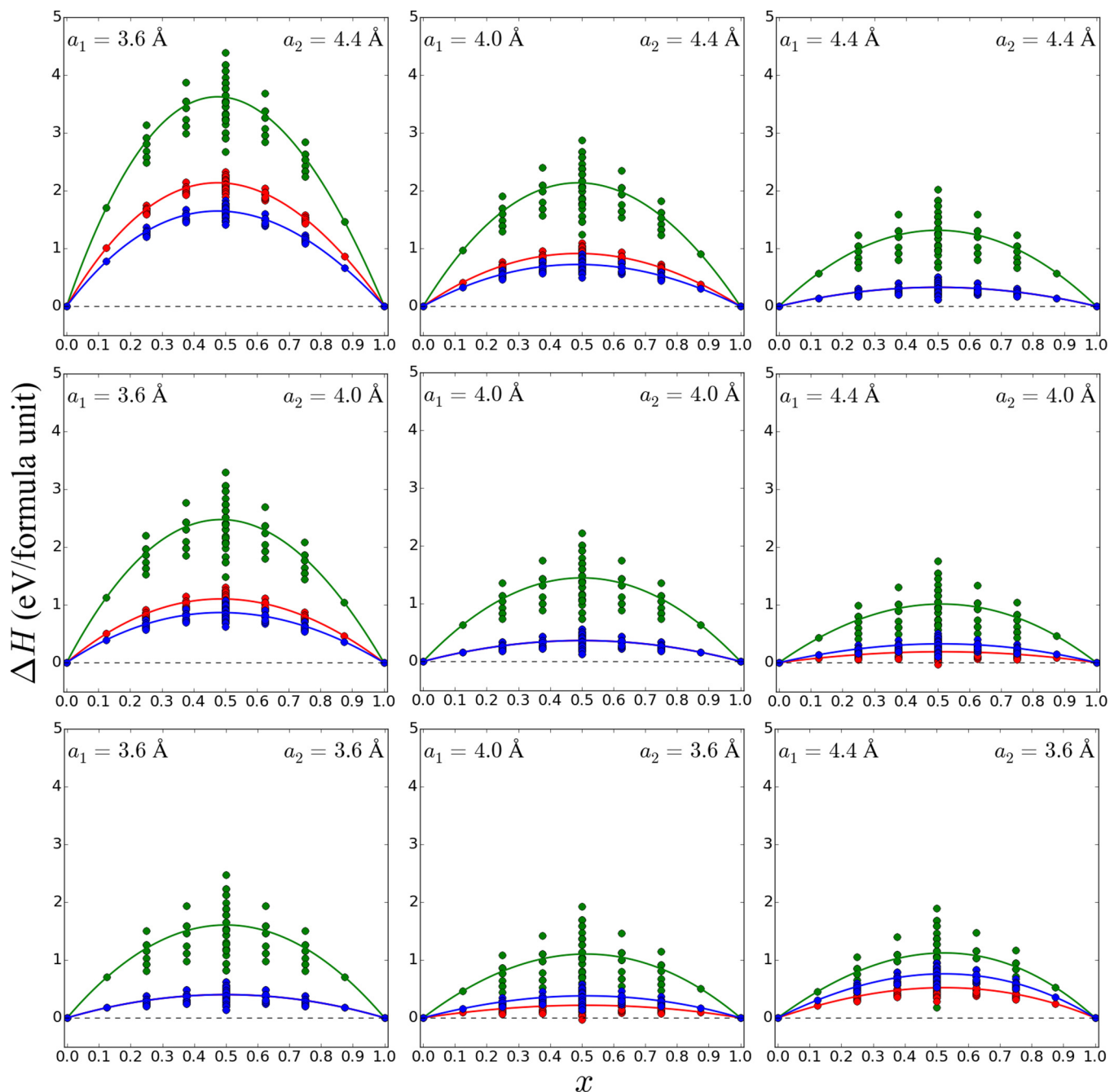
FIG. 2. Alloy mixing enthalpy as a function of the composition and the lattice constants of the pure compounds. The symbols represent the values calculated for the different configurations and the solid lines the mixing enthalpy of the random alloy, determined using Eq. (6). The color scheme is the same as in Fig. 1, with the red, green, and blue points representing the $(I,V)O_3$-$(II,IV)O_3$, $(I,V)O_3$-$(III,III)O_3$, and $(II,IV)O_3$-$(III,III)O_3$ alloys, respectively.

the temperature was considered by calculating the Gibbs free energy of the system:

$$\Delta G(x,T) = \Delta H(x) - T \Delta S(x), \qquad (7)$$

where $\Delta S(x) = -2k_B[x \ln x + (1-x)\ln(1-x)]$ is the mixing entropy of an ideal solution, the factor 2 coming from the fact that the system has two cation sublattices.

(2) *Ground-state structures*. As opposed to high temperatures, at which the average enthalpy of mixing is appropriate to describe the system, at low temperatures it is necessary to identify the ground-state structures. This problem is not always

simple since the alloy can present very complex ground-state structures. The supercell used in the high-temperature analysis is too small for this task. Larger supercells could be considered, but as the total number of configurations increases exponentially with the number of cations, the direct search of nonequivalent configurations becomes impractical, even taking into account symmetry arguments, and a heuristic method should be employed, such as simulated annealing or a genetic algorithm. In this work, we followed a different approach, and used the method of derivative superstructures developed by Hart *et al.* [42]. Through this method it is

TABLE II. Fitting parameters (in eV/formula unit) of the random alloy mixing enthalpy [Eq. (6)], calculated for alloys with lattice constants a_1 and a_2 shown in Fig. 2.

	$(I,V)O_3$-$(II,IV)O_3$ alloy					
	$a_1 = 3.6\,\text{Å}$		$a_1 = 4.0\,\text{Å}$		$a_1 = 4.4\,\text{Å}$	
	α	β	α	β	α	β
$a_2 = 3.6\,\text{Å}$	3.28	0.00	1.68	0.19	3.82	0.85
$a_2 = 4.0\,\text{Å}$	9.47	−0.95	2.95	0.00	1.47	0.15
$a_2 = 4.4\,\text{Å}$	19.1	−4.38	7.80	−0.71	2.68	0.00
	$(I,V)O_3$-$(III,III)O_3$ alloy					
	$a_1 = 3.6\,\text{Å}$		$a_1 = 4.0\,\text{Å}$		$a_1 = 4.4\,\text{Å}$	
	α	β	α	β	α	β
$a_2 = 3.6\,\text{Å}$	13.1	0.00	8.53	0.95	8.23	1.83
$a_2 = 4.0\,\text{Å}$	21.3	−2.13	11.8	0.00	7.88	0.79
$a_2 = 4.4\,\text{Å}$	32.5	−5.91	18.3	−1.66	10.7	0.00
	$(II,IV)O_3$-$(III,III)O_3$ alloy					
	$a_1 = 3.6\,\text{Å}$		$a_1 = 4.0\,\text{Å}$		$a_1 = 4.4\,\text{Å}$	
	α	β	α	β	α	β
$a_2 = 3.6\,\text{Å}$	3.27	0.00	2.94	0.33	5.57	1.24
$a_2 = 4.0\,\text{Å}$	7.44	−0.74	2.95	0.00	2.53	0.25
$a_2 = 4.4\,\text{Å}$	14.8	−2.69	6.18	−0.56	2.68	0.00

possible to generate configurations of the alloy considering supercells with different sizes but also different shapes, which considerably increases the number of nonequivalent configurations found, even for small supercells. We searched the space of all the superstructures with sizes varying from two up to 16 times the size of the parent primitive cell,

which resulted in 188 729 nonequivalent configurations. For a given composition, the most stable state must be the one with lowest formation energy. However, considering different compositions, not all the lowest states are stable against phase separation into neighboring compositions. The ground states were determined by building the convex hull, using the python algorithm *ConvexHull* [43].

III. RESULTS AND DISCUSSION

A. Random alloy

In Fig. 2, we show the calculated mixing enthalpies for the three types of point-charge alloys and nine combinations of lattice constants a_1 and a_2. The mixing enthalpy of the alloy (solid lines in Fig. 2) is always positive, but its magnitude varies considerably depending on the alloy type and the lattice constants of the end pure compounds. Comparing the three types of alloys, we see that $(I,V)O_3$-$(II,IV)O_3$ and $(II,IV)O_3$-$(III,III)O_3$ have mixing enthalpies in about the same range of magnitude. On the other hand, $(I,V)O_3$-$(III,III)O_3$ has much higher mixing enthalpy when compared with the two other alloys. This means that the larger the difference in charges of cations, the less stable should be the alloy. A similar result has already pointed out by Xu *et al.* [11]. Although the $(I,V)O_3$-$(III,III)O_3$ alloy has the highest values of alloy mixing enthalpy, it has also the most spread values of mixing enthalpy for the individual configurations, and some ordered structures could have even lower values than the same structure in the other alloys, as it happens when $a_1 = 4.4\,\text{Å}$ and $a_2 = 3.6\,\text{Å}$. When the two lattice constants are equal, the $(I,V)O_3$-$(II,IV)O_3$ and $(II,IV)O_3$-$(III,III)O_3$ alloys have exactly the same mixing enthalpy, which makes sense, since when there is no internal strain, the only contribution for the instability of the alloys
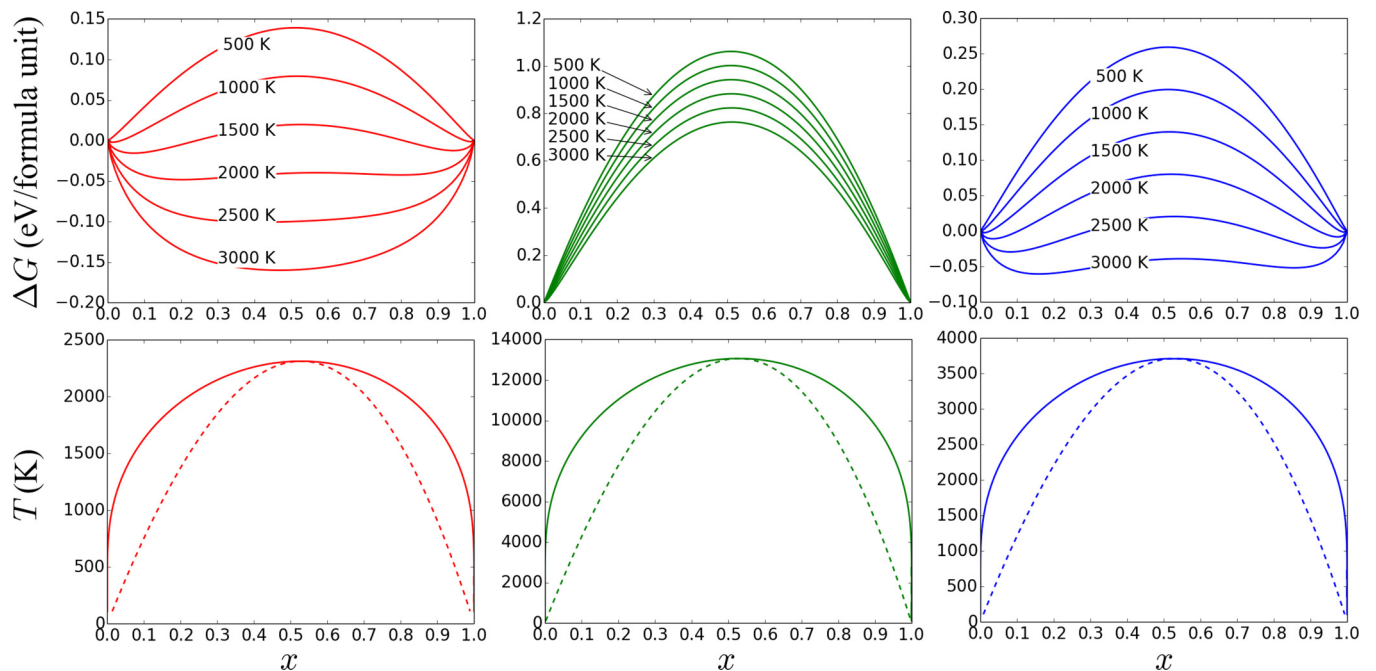

FIG. 3. Top: variation of the Gibbs free energy of the alloy as a function of the composition and temperature. Bottom: phase diagrams of the alloys, the solid and dashed lines being the binodal and spinodal lines, respectively. Red: $(I,V)O_3$-$(II,IV)O_3$; green: $(I,V)O_3$-$(III,III)O_3$; blue: $(II,IV)O_3$-$(III,III)O_3$. The lattice constants are $a_1 = 4.1\,\text{Å}$ and $a_2 = 3.8\,\text{Å}$.

comes from the charge differences, which are the same for these alloys. When $a_1 < a_2$, the $(II,IV)O_3$-$(III,III)O_3$ alloy has lower mixing enthalpy than the $(I,V)O_3$-$(II,IV)O_3$ alloy and the opposite happens when $a_1 > a_2$.

We also note in Fig. 2 that the alloy mixing enthalpies are near symmetric in relation to $x = 0.5$. In order to analyze the deviation from the regular solution behavior, we present the fitting parameters of Eq. (6) in Table II. For the three types of alloys, the parameter β is zero only when the lattices constants a_1 and a_2 are equal, so the mixing enthalpies are strictly symmetric only in these situations. As the difference between the lattice constants of the end compounds increases, the parameter Ω in Eq. (6) becomes more dependent on the alloy composition and the mixing enthalpy of the alloy is less symmetric. The asymmetry reflects the relative difference between the lattice constants, i.e., β is negative when $a_1 < a_2$ and positive when $a_1 > a_2$.

In Fig. 3, we show how the Gibbs free energy varies with the alloy composition and temperature for the specific lattice constants $a_1 = 4.1$ Å and $a_2 = 3.8$ Å. As well as the enthalpy of mixing, the free energy is almost symmetric in relation to $x = 0.5$. Even considering a screening of the Coulomb interaction, none of the alloys are stable at room temperature, which can be seen by the downward concavity of the free energy at low temperatures. As the temperature increases, the binodal points, i.e., points in which the free-energy curve has a common tangent, appears at about 1500 K for the $(I,V)O_3$-$(II,IV)O_3$ alloy and about 2000 K for the $(II,IV)O_3$-$(III,III)O_3$ alloy, which means that these alloys are stable against phase decompositions at these temperatures, at least for a small range of compositions. The $(I,V)O_3$-$(III,III)O_3$ alloy maintains the downward shape even for high temperatures, confirming that this kind of alloy is less stable than the other two ones. In order to make this difference clearer, we built the phase diagrams of the alloys, which are also shown in Fig. 3. The comparison of the three alloys can be done in terms of the critical temperature, i.e., the temperature above which the alloy is stable against phase separation for the entire range of compositions. For these specific lattice constants, the critical temperatures of the $(I,V)O_3$-$(II,IV)O_3$, $(II,IV)O_3$-$(III,III)O_3$, and $(I,V)O_3$-$(III,III)O_3$ alloys are 2312, 3711, and 13053 K, respectively. These hypothetical critical temperatures are, of course, very high since only Coulomb energy was considered.

In order to better understand the dependence of the Gibbs free energy on the alloy lattice constants, we repeated the calculations for a grid of points with a_1 and a_2 varying from 3.5 to 4.5 Å, in intervals of 0.1 Å, which covers the range of experimental lattice constants of cubic perovskite compounds. To easily compare the different alloys, we show only the free energy for the composition $x = 0.5$. The calculations were done at a temperature of 300 K. After calculating the free energy over the discrete grid of points, the data were interpolated using a cubic spline form. The results are presented using color mapping in Fig. 4. We see that, for all the three types of alloys, for a fixed lattice constant a_2, the free energy decreases when a_1 increases, reaches a minimum value, and then increases again. For none of the alloys this minimum of free energy happens when the lattice constants of the pure compounds a_1 and a_2 are the
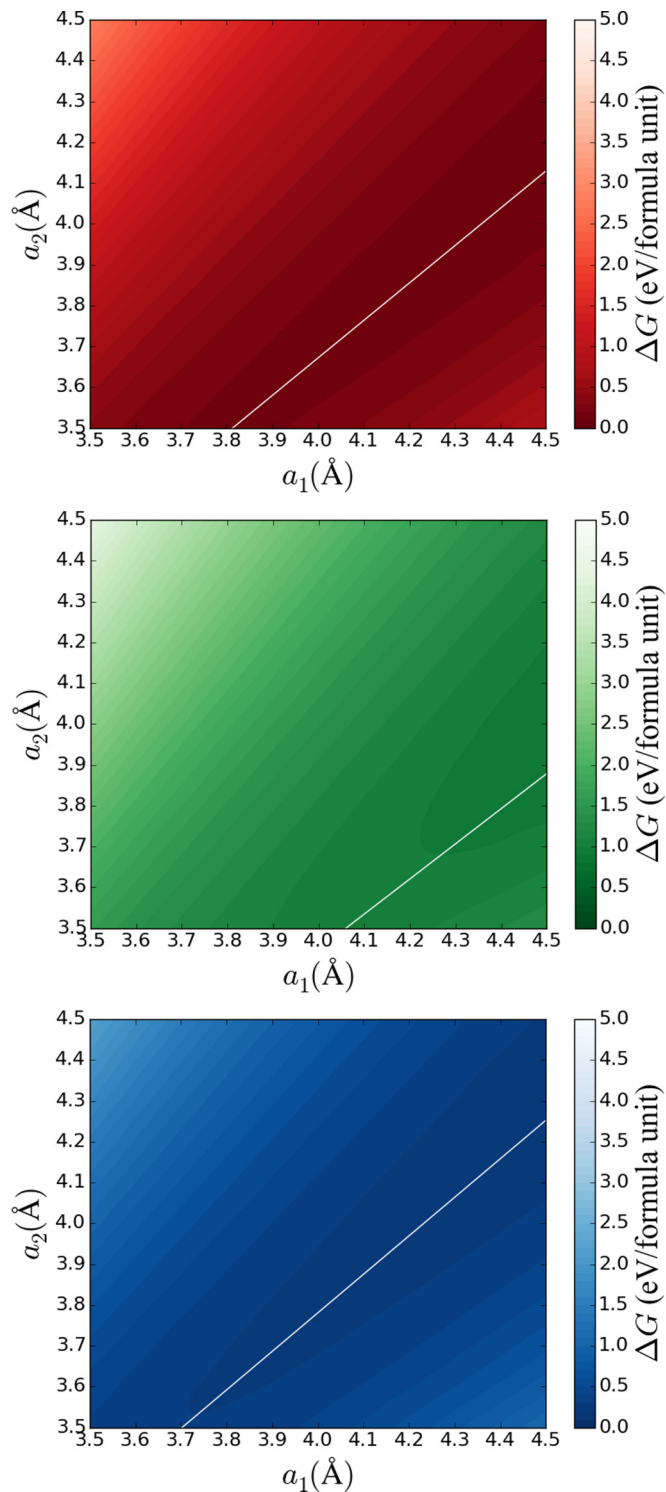

FIG. 4. Variation of the Gibbs free energy of the alloy with composition $x = 0.5$ and temperature $T = 300$ K as a function of the lattice constants a_1 and a_2. The energy scales are the same, but the colors distinguish the three types of alloys. Top: $(I,V)O_3$-$(II,IV)O_3$. Middle: $(I,V)O_3$-$(III,III)O_3$. Bottom: $(II,IV)O_3$-$(III,III)O_3$. The white lines represent the linear relations that minimize the free energies (Table III).

same, which should be expected for homovalent alloys, for which usually the smaller the mismatch between the pure compounds, the more stable the alloy [44,45]. Instead, there

TABLE III. Relations between the lattice constants which minimize the Gibbs free energy of the random alloys with composition $x = 0.5$ and temperature $T = 300$ K.

Type	Expression
$(I,V)O_3$-$(II,IV)O_3$	$a_2 = 0.918a_1$
$(I,V)O_3$-$(III,III)O_3$	$a_2 = 0.862a_1$
$(II,IV)O_3$-$(III,III)O_3$	$a_2 = 0.945a_1$

is a linear relation between the combination a_1 and a_2 that minimizes the free energy (Table III). Comparing the three alloys, as already had been seen in Fig. 2 for the enthalpy of mixing, $(I,V)O_3$-$(III,III)O_3$ presents higher free energy than the other two alloys. Moreover, the minimum energy line of $(I,V)O_3$-$(III,III)O_3$ alloy has a smaller slope, which means that the line is farther from the $a_1 = a_2$ relation. This behavior suggests that a larger mismatch between lattice constants is necessary to compensate the large difference of charge between the cations of this alloy. As we will show in the next section, the alloys present the tendency of spontaneous
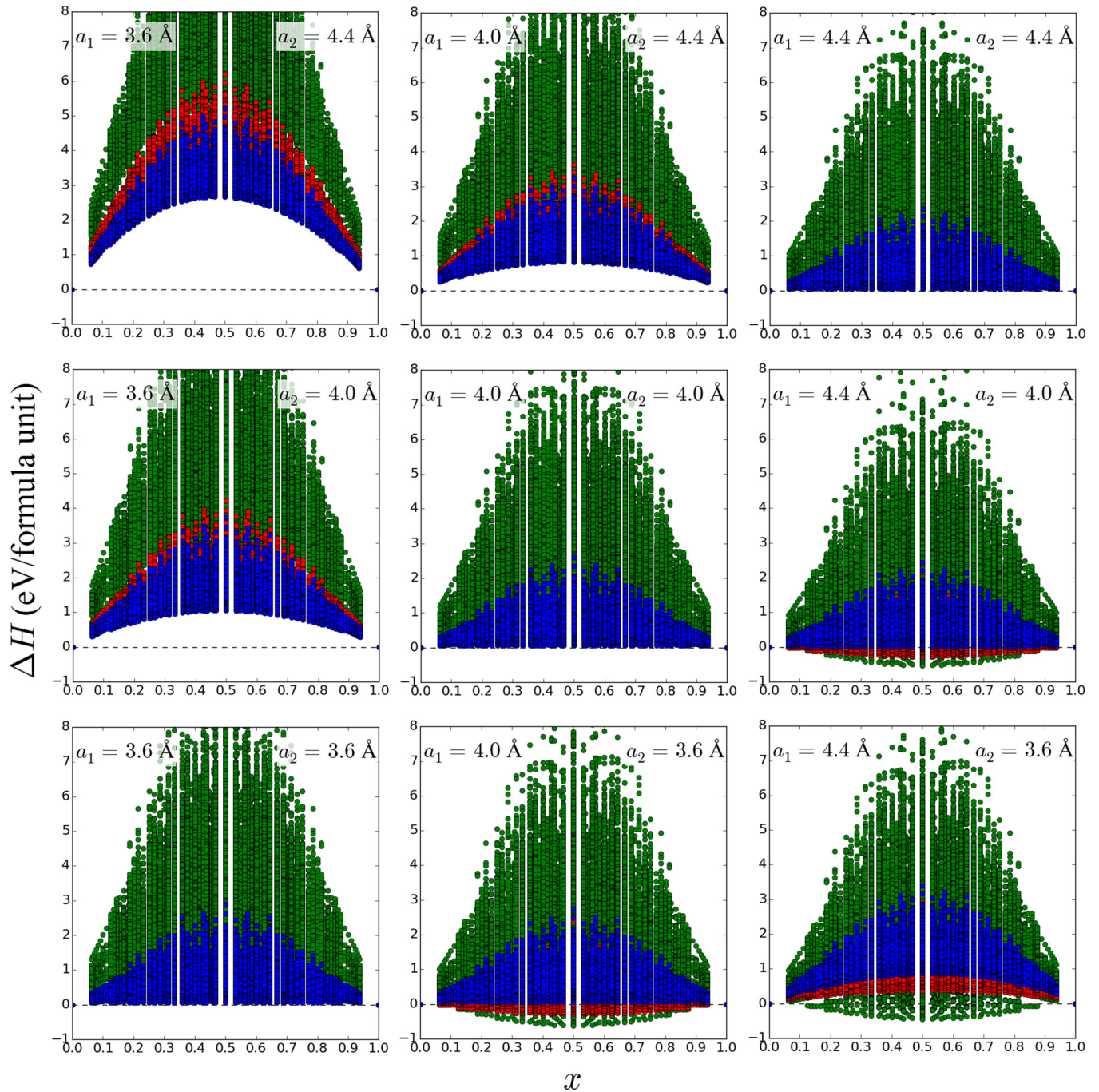

FIG. 5. Mixing enthalpy in terms of the alloy composition and the lattice constants calculated for the configurations generated through the derivative structures method. Red, green, and blue points represent the $(I,V)O_3$-$(II,IV)O_3$, $(I,V)O_3$-$(III,III)O_3$, and $(II,IV)O_3$-$(III,III)O_3$ alloys, respectively.
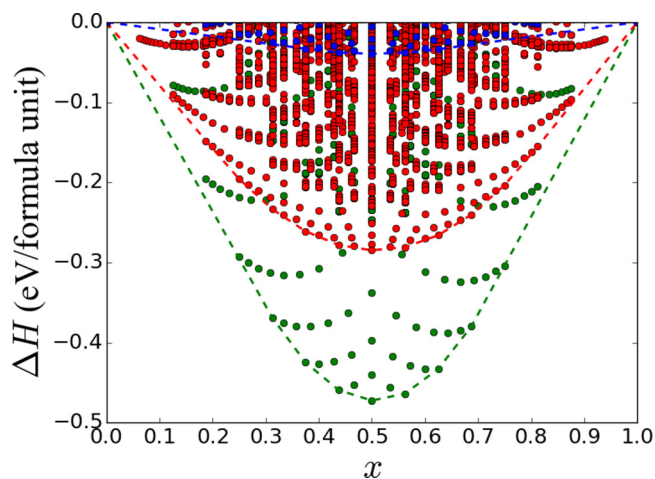
FIG. 6. Mixing enthalpy as a function of the composition for the alloys with lattice constants $a_1 = 4.1$ Å and $a_2 = 3.8$ Å. Only the negative values are shown. The dashed lines represent the convex hulls. Red, green, and blue points represent the $(I,V)O_3$-$(II,IV)O_3$, $(I,V)O_3$-$(III,III)O_3$, and $(II,IV)O_3$-$(III,III)O_3$ alloys, respectively.

ordering in the region of lowest free energy showed in Fig. 4. The formation of ordered structures might be related to the decrease of the free energy. Zunger *et al.*, e.g., showed that even large lattice-mismatch isovalent alloys can present spontaneous ordering under certain conditions [46,47].

B. Ground-state structures

We calculated the mixing enthalpies of all the 188 729 configurations for the three types of alloys again considering nine different combinations of the lattice constants a_1 and a_2. The results are shown in Fig. 5. The average behavior of the mixing enthalpy is similar to that presented in Fig. 2 but, as the number of configurations is now much larger, configurations with higher and lower mixing enthalpies can be reached. Here, we are only interested in the configurations with the lowest mixing enthalpies. We note that the combinations of a_1 and a_2 that lead to high mixing enthalpy of the random alloy in Figs. 2 and 4 do not have configurations with negative mixing enthalpy, so at low temperatures the alloys should phase separate into the end pure compounds ABO_3 and $A'B'O_3$. When $a_1 = a_2$, the $(I,V)O_3$-$(II,IV)O_3$ and $(II,IV)O_3$-$(III,III)O_3$ alloys have the same mixing enthalpies and the minimum values are close to zero (about 0.05 eV/formula unit), but do not form a convex hull. For the $(I,V)O_3$-$(III,III)O_3$ alloy, the minimum mixing enthalpies are about 0.2 eV/formula unit. When the lattice constants are closer to the minimum lines in Fig. 4, the alloys can have configurations with negative mixing enthalpy, as happens when $a_1 = 4.0$ Å and $a_2 = 3.6$ Å in Fig. 5. These configurations should be more stable than the end pure compounds, but not always stable against phase separation since they can be less stable than other configurations with close compositions.

With the purpose of analyzing the ground-state configurations, from this point on, we consider only the alloys with end point lattice constants $a_1 = 4.1$ Å and $a_2 = 3.8$ Å. In Fig. 6, we show only the negative values of the mixing enthalpies of the alloys. Based on these values, we built convex hulls
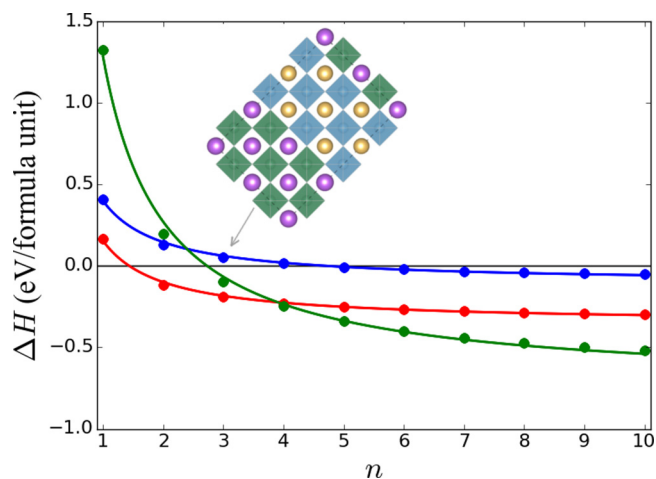

FIG. 7. Variation of the mixing enthalpy of the structures with alternating layers perpendicular to [110] direction as a function of the number of cationic planes in each layer (symbols). The solid lines are fitting curves given by Eq. (8). Red, green, and blue points represent the $(I,V)O_3$-$(II,IV)O_3$, $(I,V)O_3$-$(III,III)O_3$, and $(II,IV)O_3$-$(III,III)O_3$ alloys, respectively. The inset illustrates a structure with three planes of cations in each layer.

that are formed by those points that are stable with respect to separation into two configurations at neighboring compositions. It was verified that the points that form the convex hull, for the three alloys, correspond to structures formed by layers perpendicular to the crystal direction [110], with alternating ABO_3 and $A'B'O_3$, the thickness of the layers depending on the composition of the alloy. As the number of atomic planes in each layer increases, the mixing energy becomes more negative and the convex hull decreases. This behavior can be verified considering only the mixing enthalpy for the composition $x = 0.5$. Figure 7 shows the variation of mixing enthalpy with the number of planes in each layer. The mixing enthalpy of the $(I,V)O_3$-$(II,IV)O_3$ and $(II,IV)O_3$-$(III,III)O_3$ alloys have very similar variation, with the former always more negative. For thin layers, the $(I,V)O_3$-$(III,III)O_3$ alloy has higher mixing enthalpy than the other ones but, as the layer thickness increases, the $(I,V)O_3$-$(III,III)O_3$ mixing enthalpy becomes the lowest. For the three alloys, the ground-state mixing enthalpy can be fitted using an expression of the type

$$\Delta H = \frac{C}{n} + D, \qquad (8)$$

where n is the number of cationic planes in each layer and the fitting parameters C and D depend on the alloy type and the lattice constants. The absence of a minimum for the mixing enthalpy indicates that the alloys tend to phase separate at low temperatures, as was already pointed out in the phase-diagram analysis.

Finally, we analyzed different ordered structures for the alloys with composition $x = 0.5$, which means the double perovskites $AA'BB'O_6$. We consider three different patterns of ordered structures [17]: layered, columnar, and rock salt, which correspond to structures with layers perpendicular to [001], [110], and [111] directions, respectively. Structures in which the cation types A/A' and B/B' are ordered in the same
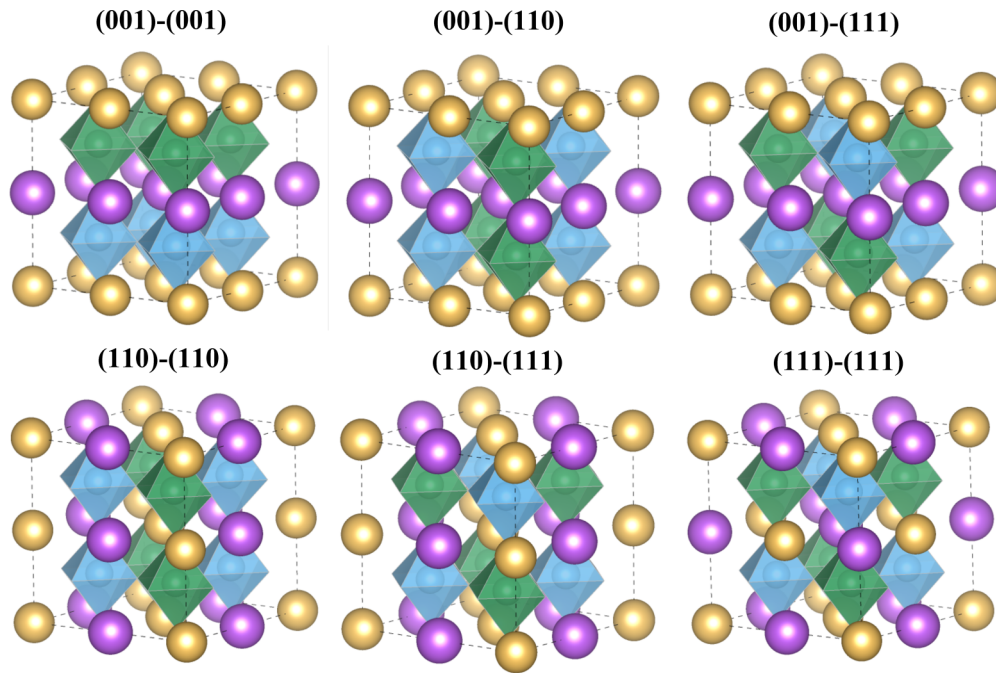
FIG. 8. Six different types of ordered structures for $AA'BB'O_6$ that were analyzed in this work. The labels refer to the ordering plane of the two sublattices: $(h_Ak_Al_A)$-$(h_Bk_Bl_B)$. The large spheres are the cations in sublattice A/A', the spheres inside the octahedra represent the cations in sublattice B/B'.

and different directions were considered. We use the notation $(h_Ak_Al_A)$-$(h_Bk_Bl_B)$ to refer to a structure in which the cations in A/A' sublattice form layers parallel to $(h_Ak_Al_A)$ and the cations in B/B' sublattice form layers parallel to $(h_Bk_Bl_B)$. As we only consider electrostatic interactions among the cations, a structure like (001)-(110) must have the same energy as (110)-(001) structure due to the crystal symmetry. Figure 8 illustrates the six possible ordered structures. We calculated the mixing enthalpies of these structures in relation to the pure compounds, again considering the lattice constants $a_1 = 4.1\,\text{Å}$ and $a_2 = 3.8\,\text{Å}$. The results are shown in Fig. 9. We see that the three types of alloys have similar sequences of mixing enthalpies for the ordered structures. The only apparent difference is the magnitude of the mixing enthalpies, which in $(I,V)O_3$-$(III,III)O_3$ is about five times larger than in the other alloys. We begin comparing structures with one cationic plane in each sublattice per layer. In this case, the structure with lowest mixing enthalpy is (111)-(111), i.e., in which the cations in the two sublattices form rock-salt patterns. The sequence of structures, in ascending order of mixing enthalpies, is (110)-(111), (110)-(110), (001)-(111), (001)-(110), and (001)-(001). We notice that the tendency of rock-salt/layered ordering [17], i.e., (111)-(100) structure, is not observed, if only considering Coulomb interactions. As the number of cationic planes in the layers increases, the structure with both sublattices ordered in (110) planes becomes the one with lowest mixing enthalpies. The decrease of mixing enthalpy of the (110)-(110) structure has already been shown in Fig. 7. This is also the only structure for which the mixing enthalpy decreases when the layer thickness increases. All the other structures present an increase of mixing enthalpy when the number of cationic planes per layer increases. It is possible to observe that, although increasing, the variations of

mixing enthalpies of structures with both sublattices ordering in the same direction are not large and converge to values of few eV/formula unit. On the other hand, for structures with different ordered patterns in the two sublattices, the formation energy increases considerably with the thickness of the layers, in a variation that seems exponential.

Let us analyze the superlattice tendency in terms of formal charges of the atomic planes. A (001)-oriented superlattice is
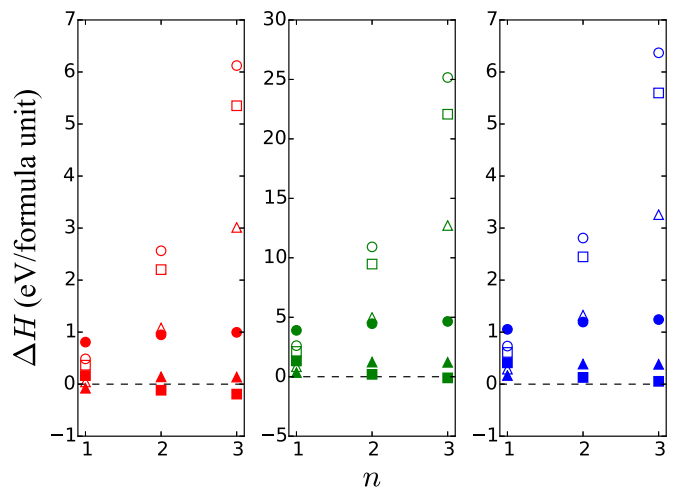

FIG. 9. Mixing enthalpies of ordered structures with different orientations as a function of the number of cationic planes per layer. The symbols represent the following structures: (001)-(001) (full circles), (001)-(110) (empty circles), (001)-(111) (empty squares), (110)-(110) (full squares), (110)-(111) (empty triangles), and (111)-(111) (full triangles). Left: $(I,V)O_3$-$(II,IV)O_3$. Middle: $(I,V)O_3$-$(III,III)O_3$. Right: $(II,IV)O_3$-$(III,III)O_3$.

TABLE IV. Charge per two-dimensional unit cell (in atomic units) for different superlattice directions and different atomic layers.

	[001]		[110]		[111]	
	AO	BO_2	ABO	O_2	AO_3	B
(I,V)O_3	-1	$+1$	$+4$	-4	-5	$+5$
(II,IV)O_3	0	0	$+4$	-4	-4	$+4$
(III,III)O_3	$+1$	-1	$+4$	-4	-3	$+3$

formed by alternating AO and BO_2 layers. On the other hand, a (110) superlattice presents a sequence of ABO and O_2 layers. Finally, a (111) superlattice is formed by AO_3 and B layers. As we are considering three types of perovskite compound, the surface charge can be different, even considering the same direction of ordering, as we show in Table IV. We see that, when a superlattice is formed along the [110] direction, the surface charges at both sides of the interface between ABO_3 and $A'B'O_3$ have the same magnitude but opposite signs, so the net charge at the interface is null. It means that there is no polarity discontinuity at the interface between the two layers in (110) superlattices, and the system should be electrostatically stable [48]. On the other hand, in (100) and (111) structures, as the net surface charge is not null at the interface, there is a polarity discontinuity, which results in an internal electric field along the superlattice, contributing to increase the Coulomb energy of the system. This kind of phenomenon has been largely studied for both ionic and semiconductor surfaces [48–50]. The influence of the local non-null charge in the interfaces is more significant when the thickness of the layers increases, since for thin layers ($n = 1$), (111) superlattices have lower mixing enthalpies than the (110) ones. A very similar result was found by Deng *et al.* in (III,V)/(II,VI) semiconductor superlattices [51,52]. It is important to point out that we only considered in this study the regular stacking of planes in the perovskite structure. Nonregular stacking sequences could have lower electrostatic energy than the regular one. As an example, the structure formed by the sequence of planes AO-BO_2-$B'O_2$-$A'O$ along the [001] direction has lower energy than the AO-BO_2-$A'O$-$B'O_2$ regular structure. However, more detailed analysis is beyond the scope of this work.

IV. CONCLUSIONS

We analyzed how the lattice constants of the pure compounds ABO_3 and $A'B'O_3$ can influence the stability of the

alloy formed when they are mixed. The mixing enthalpy of the random alloy is minimized when the two lattice constants follow a linear relationship, but are not the same, as is usually observed in homovalent alloys. The larger the difference in formal charge of the cations, the farther the lattice constant relation from that of homovalent alloys. This means that the difference of charges between the mixing cations has a role as important in the stability of quaternary perovskite alloys as the lattice mismatch. We also observed that alloys with greater difference in formal charge between the cations should have higher formation energies. So, the (I,V)O_3-(III,III)O_3 alloys should be less stable than the (I,V)O_3-(II,IV)O_3 and (II,IV)O_3-(III,III)O_3 ones. We noted that the ground-state configurations of these alloys consist of superlattices with alternated layers along [110] direction. We compared the formation energies of six different ordering structures and showed that structures with the same direction of ordering in both sublattices in general are more stable than those with a different pattern in each sublattice. When considering only one cationic plane per layer, the structure with lowest formation energy is rock-salt ordered but, with the increasing of the layer thickness, the columnar structure becomes the most stable. If verified, the tendency to (110) ordering of perovskite alloys could have important implications on technological applications, such as for example in ionic transport, given the sensibility of the mobility of oxygen vacancies with cation ordering in perovskites [53]. As the alloys are simulated as point charges, the work elucidates the contribution of electrostatic interaction to the stability of quaternary alloys. To better understand the complexity of the real solid solutions, other contributions to the free energy must be considered, aside from structural relaxations, vibrational entropy at finite temperatures, and the role of point and extended defects.

[1] E. Dagotto, T. Hotta, and A. Moreo, Phys. Rep. **344**, 1 (2001).

[2] N. Izyumskaya, Y. Alivov, and H. Morkoç, Crit. Rev. Solid State Mater. Sci. **34**, 89 (2009).

[3] J. B. Goodenough, Rep. Prog. Phys. **67**, 1915 (2004).

[4] K. Kreuer, Annu. Rev. Mater. Res. **33**, 333 (2003).

[5] W. Wang, M. O. Tadé, and Z. Shao, Chem. Soc. Rev. **44**, 5371 (2015).

[6] F. Dogan, H. Lin, M. Guilloux-Viry, and O. Peña, Sci. Technol. Adv. Mater. **16**, 020301 (2015).

[7] A. R. West, *Solid State Chemistry and its Applications* (Wiley, Chichester, 2014), pp. 54–57.

[8] S. K. Mishra, N. Choudhury, S. L. Chaplot, P. S. R. Krishna, and R. Mittal, Phys. Rev. B **76**, 024110 (2007).

[9] L. Bellaiche, J. Padilla, and D. Vanderbilt, Phys. Rev. B **59**, 1834 (1999).

[10] R. Armiento, B. Kozinsky, G. Hautier, M. Fornari, and G. Ceder, Phys. Rev. B **89**, 134103 (2014).

[11] H. Xu, A. Navrotsky, Y. Su, and M. L. Balmer, Chem. Mater. **17**, 1880 (2005).

[12] A. Fuertes, J. Mater. Chem. **22**, 3293 (2012).

[13] H. Chen and N. Umezawa, Phys. Rev. B **90**, 045119 (2014).

[14] M. T. Anderson, K. B. Greenwood, G. A. Taylor, and K. R. Poeppelmeiert, Prog. Solid State Chem. **22**, 197 (1993).

[15] M. C. Knapp and P. M. Woodward, J. Solid State Chem. **179**, 1076 (2006).

[16] P. K. Davies, H. Wu, A. Y. Borisevich, I. E. Molodetsky, and L. Farber, Annu. Rev. Mater. Res. **38**, 369 (2008).

[17] G. King and P. M. Woodward, J. Mater. Chem. **20**, 5785 (2010).

[18] A. Roy and D. Vanderbilt, Phys. Rev. B **83**, 134116 (2011).

[19] N. G. Zamkova, V. S. Zhandun, and V. I. Zinenko, Phys. Status Solidi B **250**, 1888 (2013).

[20] S. Vasala and M. Karppinen, Prog. Solid State Chem. **43**, 1 (2015).

[21] L. Bellaiche and D. Vanderbilt, Phys. Rev. Lett. **81**, 1318 (1998).

[22] Z. Wu and H. Krakauer, Phys. Rev. B **63**, 184113 (2001).

[23] T. Takahashi, E. J. Wu, A. V. D. Ven, and G. Ceder, Jpn. J. Appl. Phys. **39**, 1241 (2000).

[24] V. Stevanović, M. d'Avezac, and A. Zunger, J. Am. Chem. Soc. **133**, 11649 (2011).

[25] A. Seko and I. Tanaka, Phys. Rev. B **91**, 024106 (2015).

[26] R. Magri, S.-H. Wei, and A. Zunger, Phys. Rev. B **42**, 11388 (1990).

[27] T. Hungría, M. Algueró, and A. Castro, Chem. Mater. **18**, 5370 (2006).

[28] J. Narkilahti, M. Plekh, J. Levoska, and M. Tyunina, Phys. Rev. B **79**, 014106 (2009).

[29] P. A. Markovin, V. V. Lemanov, M. E. Guzhva, P. P. Syrnikov, and T. A. Shaplygina, Phys. Solid State **56**, 989 (2014).

[30] Y. Hamazaki, W. Sakamoto, M. Moriya, and T. Yogo, Jpn. J. Appl. Phys. **48**, 09KA08 (2009).

[31] K. Kakimoto, I. Masuda, and H. Ohsato, Jpn. J. Appl. Phys. **43**, 6706 (2004).

[32] A. Ohtomo, J. Nishimura, Y. Murakami, and M. Kawasaki, Appl. Phys. Lett. **88**, 232107 (2006).

[33] G. Li, X. Kuang, S. Tian, F. Liao, X. Jing, Y. Uesu, and K. Kohn, J. Solid State Chem. **165**, 381 (2002).

[34] H. S. C. O'Neill and A. Navrotsky, Am. Mineral. **68**, 181 (1983).

[35] E. Takayama-Muromachi and A. Navrotsky, J. Solid State Chem. **72**, 244 (1988).

[36] R. D. Rosenstein and R. Schor, J. Chem. Phys. **38**, 1789 (1963).

[37] P. P. Ewald, Ann. Phys. **369**, 253 (1921).

[38] J. D. Gale and A. L. Rohl, Mol. Simul. **29**, 291 (2003).

[39] A. R. Denton and N. W. Ashcroft, Phys. Rev. A **43**, 3161 (1991).

[40] R. Grau-Crespo, S. Hamad, C. R. A. Catlow, and N. H. de Leeuw, J. Phys.: Condens. Matter **19**, 256201 (2007).

[41] D. R. Gaskell, *Introduction to the Thermodynamics of Materials*, 5th ed. (Taylor & Francis, New York, 2008), p. 252.

[42] G. L. W. Hart and R. W. Forcade, Phys. Rev. B **77**, 224115 (2008).

[43] K. J. Millman and M. Aivazis, Computing in Science & Engineering **13**, 9 2011.

[44] G. Stringfellow, J. Cryst. Growth **27**, 21 (1974).

[45] P. Davies and A. Navrotsky, J. Solid State Chem. **46**, 1 (1983).

[46] J. Z. Liu, G. Trimarchi, and A. Zunger, Phys. Rev. Lett. **99**, 145501 (2007).

[47] X. Zhang, G. Trimarchi, M. d'Avezac, and A. Zunger, Phys. Rev. B **80**, 241202 (2009).

[48] J. Goniakowski, F. Finocchi, and C. Noguera, Rep. Prog. Phys. **71**, 016501 (2008).

[49] W. A. Harrison, E. A. Kraut, J. R. Waldrop, and R. W. Grant, Phys. Rev. B **18**, 4402 (1978).

[50] N. C. Bristowe, P. Ghosez, P. B. Littlewood, and E. Artacho, J. Phys.: Condens. Matter **26**, 143201 (2014).

[51] H.-X. Deng, J.-W. Luo, and S.-H. Wei, Phys. Rev. B **91**, 075315 (2015).

[52] H.-X. Deng, B. Huang, and S.-H. Wei, Comput. Mater. Sci. **98**, 340 (2015).

[53] B. P. Uberuaga and G. Pilania, Chem. Mater. **27**, 5020 (2015).

[54] Data access statement: a repository of the structures used in this work is available online at https://github.com/ccaetano/electrostatic-perovskite-alloys